Decoupling of the antiferromagnetic and insulating states in Tb-doped Sr_2IrO_4

J. C. Wang,[1,2,3] S. Aswartham,[1] Feng Ye,[2,1] J. Terzic,[1] H. Zheng,[1] Daniel Haskel,[4] Shalinee Chikara,[5] Yong Choi,[4] P. Schlottmann,[6] Radu Custelcean,[7] S. J. Yuan,[1] and G. Cao[1,*]

[1]*Center for Advanced Materials and Department of Physics and Astronomy, University of Kentucky, Lexington, Kentucky 40506, USA*
[2]*Quantum Condensed Matter Division, Oak Ridge National Laboratory, Oak Ridge, Tennessee 37831, USA*
[3]*Department of Physics, Renmin University of China, Beijing, China*
[4]*Advanced Photon Source, Argonne National Laboratory, Argonne, Illinois 60439, USA*
[5]*National High Magnetic Field Laboratory, Los Alamos National Laboratory, Los Alamos, New Mexico 87545, USA*
[6]*Department of Physics, Florida State University, Tallahassee, Florida 32306, USA*
[7]*Chemical Science Division, Oak Ridge National Laboratory, Oak Ridge, Tennessee 37831, USA*

(Received 21 September 2015; revised manuscript received 17 November 2015; published 8 December 2015)

Sr_2IrO_4 is a spin-orbit-coupled insulator with an antiferromagnetic (AFM) transition at $T_N = 240$ K. We report results of a comprehensive study of single-crystal $Sr_2Ir_{1-x}Tb_xO_4$ ($0 \leqslant x \leqslant 0.03$). This study found that a mere 3% ($x = 0.03$) of tetravalent $Tb^{4+}(4f^7)$ substituting for Ir^{4+} (rather than Sr^{2+}) completely suppresses the long-range collinear AFM transition but retains the insulating state, leading to a phase diagram featuring a decoupling of the magnetic interactions and charge gap. The insulating state at $x = 0.03$ is characterized by an unusually large specific heat at low temperatures and an incommensurate magnetic state having magnetic peaks at (0.95,0,0) and (0,0.95,0) in the neutron diffraction, suggesting a spiral or spin-density-wave order. It is apparent that Tb doping effectively changes the relative strength of the spin-orbit interaction (SOI) and the tetragonal crystal electric field and enhances the Hund's rule coupling that competes with the SOI, and destabilizes the AFM state. However, the disappearance of the AFM is accompanied by no metallic state chiefly because an energy level mismatch for the Ir and Tb sites weakens charge carrier hopping and causes a persistent insulating state. This work highlights an unconventional correlation between the AFM and insulating states in which the magnetic transition plays no critical role in the formation of the charge gap in the iridate.

DOI: 10.1103/PhysRevB.92.214411 PACS number(s): 71.30.+h

I. INTRODUCTION

Sr_2IrO_4 is a pseudospin-1/2 Heisenberg antiferromagnet (AFM) with a Néel temperature $T_N = 240$ K [1–4] and AFM exchange coupling approximately 0.1 eV [5]. This system is a prototype for physics driven primarily by a strong interplay of on-site Coulomb U and spin-orbit interaction (SOI) [2–6]. The relativistic SOI, proportional to Z^2 (Z is the atomic number), is approximately 0.4 eV in the iridate (compared to ~20 meV in $3d$ materials), and splits the t_{2g} bands into bands with $J_{\text{eff}} = 1/2$ and $J_{\text{eff}} = 3/2$, the latter having lower energy [2,3]. Since the Ir^{4+} ($5d^5$) ions provide five $5d$-electrons, four of them fill the lower $J_{\text{eff}} = 3/2$ bands, and one electron partially fills the $J_{\text{eff}} = 1/2$ band where the Fermi level E_F resides. The $J_{\text{eff}} = 1/2$ band is so narrow that even a reduced U (~0.50 eV) due to the extended nature of $5d$-electron orbitals is sufficient to open a gap (≤0.62 eV) supporting a novel insulating state [2–8]. It has become increasingly clear that the new, delicate balance between the relevant energies renders the ground state extremely susceptible to even slight changes of chemical composition [9–12].

Sr_2IrO_4 is perhaps the most intensively studied iridate thus far. The distinct energy hierarchy featuring a strong SOI along with its structural and electronic similarities to those of the celebrated La_2CuO_4 (K_2NiF_4 type, one hole per Ir or Cu ion, pseudospin- or spin-1/2 AFM, etc.) has stimulated a surge of interest in the iridates in recent years. A growing list of theoretical proposals predicts, among many SOI-coupled phenomena, novel topological states and superconductivity via electron or hole doping [5,6,13–15]. A recent study of angle-resolved photoemission exhibits a temperature and doping dependence of Fermi arcs at low temperatures via *in situ* K doping in cleaved crystal surfaces of Sr_2IrO_4, a phenomenology similar to that of the high-temperature superconducting cuprates [16]. However, superconductivity characterized by zero resistivity and diamagnetism remains elusive despite extensive experimental efforts. Nevertheless, a growing body of experimental evidence has shown that even slight electron or hole doping at either Sr or Ir sites leads to a metallic state despite the sizable energy gap (~0.62 eV) inherent in Sr_2IrO_4. Oftentimes, the AFM state vanishes upon the presence of the metallic state; however, there are exceptions in which the AFM state survives chemical doping at Sr sites and coexists with a doping-induced metallic state [9,10,17,18]. Furthermore, recent high-pressure studies of Sr_2IrO_4 suggest that the magnetic transition vanishes near 20 GPa [19] but the insulating state persists at high pressure up to 55 GPa [19,20], highlighting an unconventional correlation between the AFM state and the insulating gap. Indeed, a signature behavior of Sr_2IrO_4 is that transport properties exhibit no discernible anomaly corresponding to the AFM transition at $T_N = 240$ K [1,18,21], sharply contrasting that of other correlated materials and iridates, such as bilayered $Sr_3Ir_2O_7$ [22] and hexagonal $BaIrO_3$ [23]. It is not surprising that the unusual character of this SOI-coupled insulator has recently revitalized discussions of Mott, Mott-Hubbard, and Slater insulators, particularly the dependence of charge gap formation on magnetic interactions

*Corresponding author: cao@uky.edu

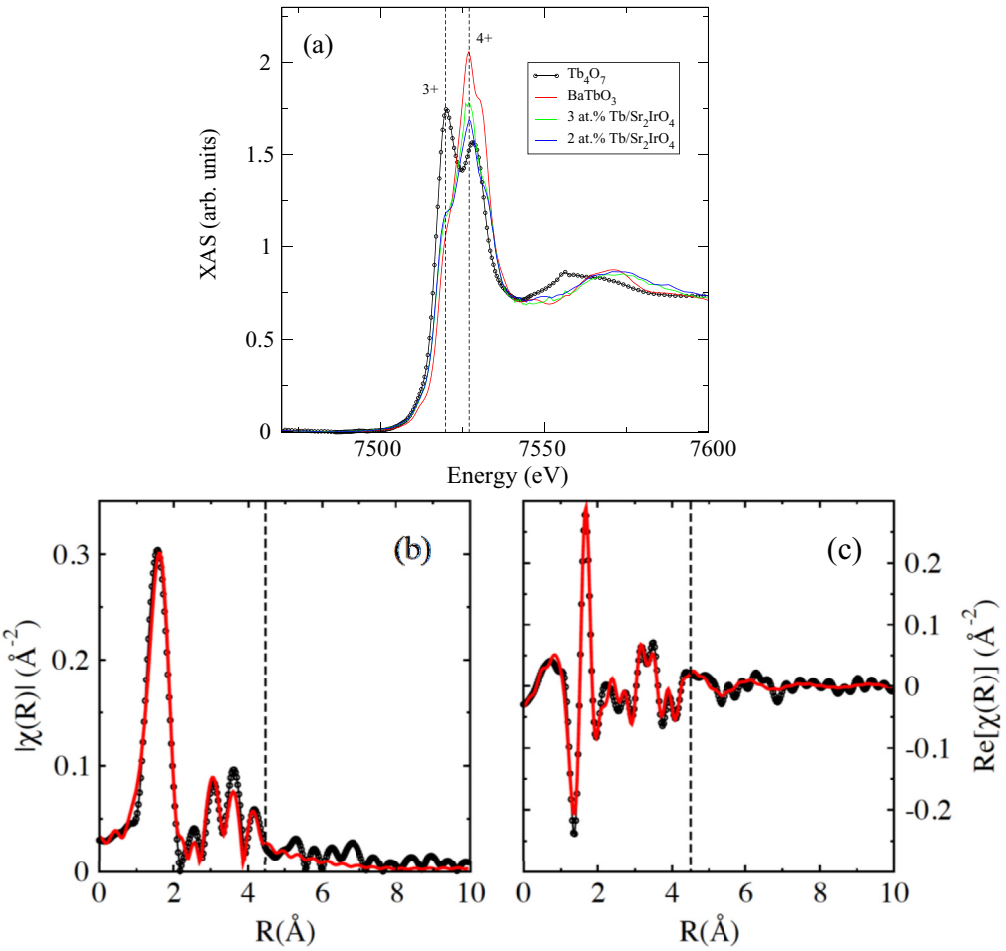

FIG. 1. (Color online) (a) A comparison of our XANES results for $x = 0.02$ and 0.03 with peaks for Tb^{3+} and Tb^{4+} ions reported in previous studies; (b) and (c) magnitudes and real parts of the complex Fourier transformation (FT) of the XAFS data (black line) and fits (red line), The XAFS data were fitted using FEFF6 theoretical standards generated with the known crystal structure of Sr_2IrO_4 at room temperature and placing Tb dopants at Ir sites. Dashed lines indicate the upper bound for the fitting range.

in Sr_2IrO_4 [24,25]. Clearly, a better understanding of the $J_{\text{eff}} = 1/2$ insulating state and its correlation with the AFM state in Sr_2IrO_4 needs to be established.

In this paper, we report results of a comprehensive study of slightly Tb-doped Sr_2IrO_4 or single-crystal $Sr_2Ir_{1-x}Tb_xO_4$ ($0 \leqslant x \leqslant 0.03$). This study utilizes various tools including x-ray absorption near-edge structure (XANES) and x-ray absorption fine structure (XAFS) spectroscopy, neutron diffraction, and other probes to characterize structural, transport, thermal, and magnetic properties of these single crystals. The central finding of this study is that a mere 3% ($x = 0.03$) tetravalent $Tb^{4+}(4f^7)$ substituting for Ir^{4+} (rather than Sr^{2+}) completely suppresses the long-range collinear AFM state but retains an insulating state, leading to a phase diagram featuring a decoupling of the magnetic interactions and charge gap. The insulating state at $x = 0.03$ exhibits an unusually large specific heat at low temperatures and accompanies an incommensurate magnetic state that is characterized by magnetic peaks at (0.95, 0, 0) and (0, 0.95, 0) in the neutron diffraction, suggesting a spiral or spin density wave order. Slight Tb doping effectively changes the relative strength of the SOI and the tetragonal crystal electric field (CEF), enhances the Hund's rule coupling that competes with the SOI, and destabilizes the AFM state; however, there is no concurrent metallic state. This "disentanglement" of the charge and magnetic aspects of doped Mott insulators sharply contrasts with the conventional argument where a simultaneous suppression of the magnetic order and charge gap would be anticipated, as both are primarily driven by the same force, the Coulomb interaction [26].

II. EXPERIMENTAL DETAILS

The single crystals studied were grown from off-stoichiometric quantities of $SrCl_2$, $SrCO_3$, IrO_2, and Tb_4O_7 using self-flux techniques [1,9–11]. The size of the single crystals is as large as $2.0 \times 2.0 \times 0.2\,\text{mm}^3$. The structures of $Sr_2Ir_{1-x}Tb_xO_4$ were determined using a Nonius Kappa CCD x-ray diffractometer at the University of Kentucky and a Rigaku x-ray diffractometer equipped with a PILATUS 200 K hybrid pixel array detector at Oak Ridge National Laboratory. Full data sets were collected between 100 and 300 K, and the structures were refined using the SHELX97-97 programs [27] and FULLPROF software [28]. The chemical compositions of the single crystals were estimated using energy-dispersive x-ray (EDX) analysis (Hitachi/Oxford 3000). The error analysis

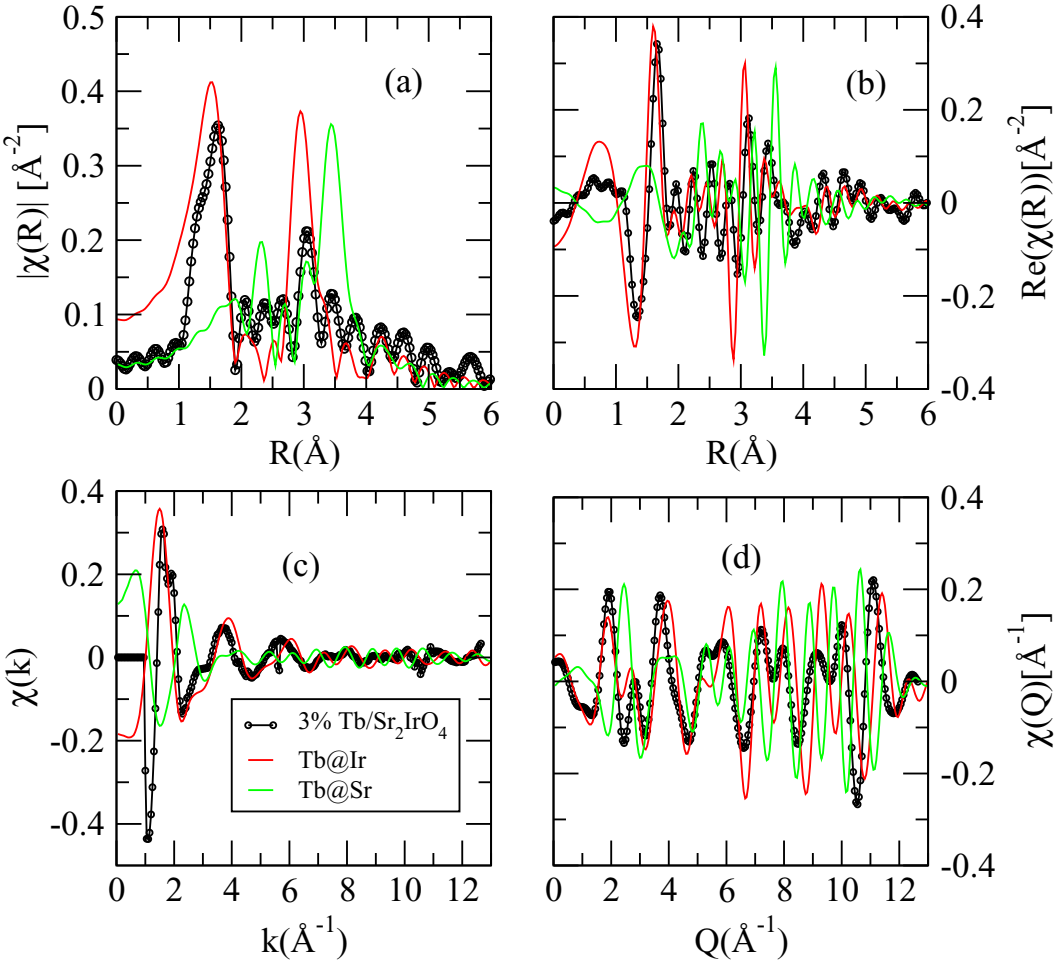

FIG. 2. (Color online) Determination of Tb site substitution by comparing XAFS data and simulations: Panels show XAFS data (black dots and lines) and simulations (red lines for Tb at Ir sites, green lines for Tb at Sr sites) for (a) the magnitude of the complex Fourier transform in real space, (b) the real part of the complex Fourier transform in real space, (c) XAFS in photoelectron momentum space, and (d) the back Fourier transform in photoelectron momentum space.Comparison of XAFS data and simulations: For Tb doping at Ir and Sr sites: Upper panels show data and simulations in real (Fourier-transformed space) while lower panels show data and simulations in photoelectron space. See text for additional details.

indicates that the error for the Sr and Ir atomic percentage is 0.1% and 3%, respectively, whereas this value for the Tb concentration is ∼11%. An example of the EDX results with standard deviation is illustrated in the Supplemental Material [29]. Magnetization, specific heat, and electrical resistivity were measured using a Quantum Design MPMS-[7] superconducting quantum interference device (SQUID) magnetometer and/or a physical Property measurement system with [14]-T field capability.

X-ray absorption near-edge structure and x-ray absorption fine structure measurements were carried out at beamline [4]-ID-D of the Advanced Photon Source, Argonne National Laboratory at room temperature. XANES data at the Tb L_3 absorption edge were used to determine the Tb valence state by comparing the leading edge position to reference samples with known valence state: Tb_4O_7 with $Tb^{3.5+}$ (i.e., mixed valence with equal amounts of 3+ and 4+ states) and $BaTbO_3$ with Tb^{4+}. XANES and XAFS data were collected in fluorescence geometry due to the low Tb content. A four-element, energy-resolving silicon drift diode detector was used to measure the intensity of the Tb $L\alpha_\alpha$ emission as the x-ray energy was scanned through the Tb $L\alpha$ absorption edge. Data were corrected for detector dead time. The reference compounds were in powder form while the Tb-doped samples were single crystals oriented in such a way that the electric field of the linearly polarized x rays was in the IrO_2 plane of the tetragonal Sr_2IrO_4 structure. XAFS data were collected to 13 $Å^{-1}$ using the same fluorescence geometry. XAFS fits were done using theoretical standards computed with the FEFF6.0 code [30]. Prior to the fittings, simulations of XAFS data were done by placing Tb atoms at either Ir or Sr sites of the Sr_2IrO_4 lattice to determine that Tb occupies Ir sites.

The neutron diffraction was carried out at Oak Ridge National Laboratory using the elastic diffuse scattering spectrometer (CORELLI) at the Spallation Neutron Source as well as triple-axis spectrometers HB1 and HB1A at the High Flux Isotope Reactor. CORELLI uses a semiwhite beam with incident neutron energy ranging from 10 to 200 meV whereas the triple-axis spectrometers HB1 and HB1A utilize

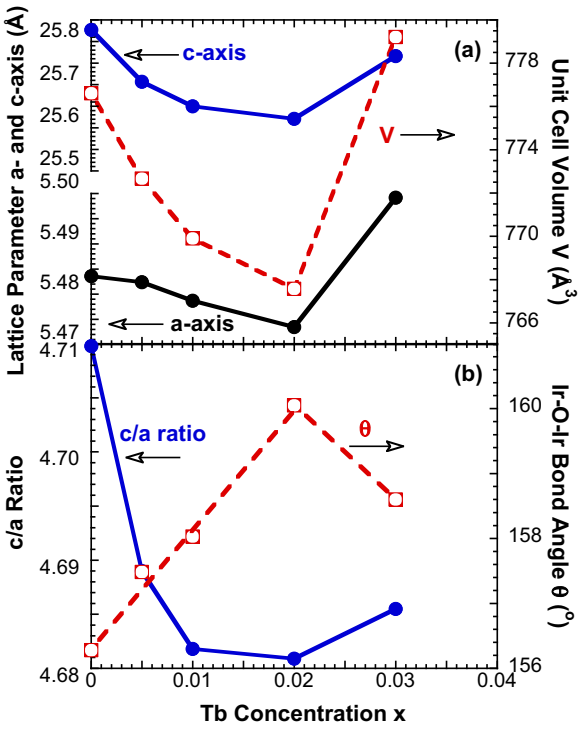

FIG. 3. (Color online) The Tb concentration dependence of (a) the a- and c-axis lattice parameters and unit cell volume V (right scale) and (b) the c/a ratio and Ir-O-Ir bond angle θ (right scale).

incident energies of 13.50 and 14.64 meV, respectively. The temperature control was achieved via a closed-cycle refrigerator.

III. RESULTS AND DISCUSSION

Rare earth ions are nominally trivalent but there are a number of exceptions, and Tb is one of them. It can be trivalent Tb^{3+}, tetravalent Tb^{4+}, or mixed-valent. The trivalent $Tb^{3+}(4f^8)$ ion has a tendency to lose its eighth $4f$ electron to become tetravalent $Tb^{4+}(4f^7)$. We therefore conducted XANES experiments to determine the valence state of Tb. The energy difference for a $2p_{3/2}$ core level electron excitation into empty $5d$ states between Tb^{3+} and Tb^{4+} ions is about 8 eV as seen in Fig. 1 [30]. A comparison of our XANES results for $x = 0.02$ and 0.03 samples with those reported for Tb^{3+} and Tb^{4+} ions [30,31] clearly indicates the presence of majority tetravalent Tb^{4+} ions in $Sr_2Ir_{1-x}Tb_xO_4$ [see Fig. 1(a)]. Furthermore, an analysis of our XAFS data leads to the conclusion that tetravalent Tb^{4+} ions substitute for Ir^{4+} ions rather than Sr^{2+} ions (see more details below). The XAFS data were fitted using FEFF6.0 theoretical standards [32] generated with the crystal structure of Sr_2IrO_4 at room temperature [33–35] and placing a Tb dopant at the Ir site (see more details below). The calculations were done with the electric field polarization in the IrO_2 plane to match experimental conditions. Data in the k range of 212 $Å^{-1}$ were Fourier transformed into real space and fitted in the range of 1.4–4.5 Å. The amplitude reduction factor S_0^2 was found to be 0.81 and an overall e_0 shift of 2.41 eV was needed to match the FEFF theory and experiment. The results are illustrated in Figs. 1(b)

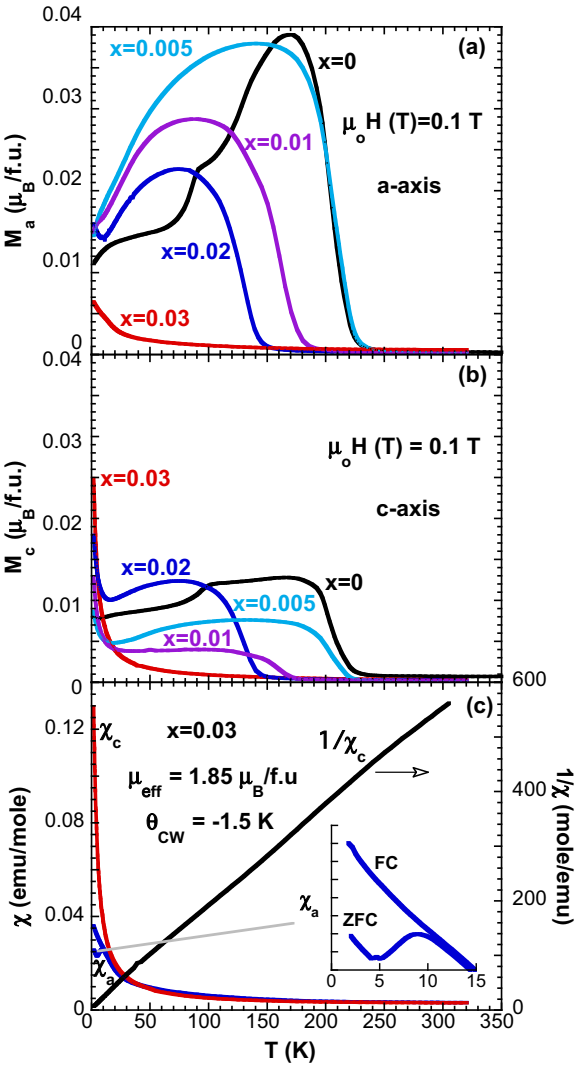

FIG. 4. (Color online) The temperature dependence at $\mu_0 H = 0.1$ T of the magnetization (a)M_a and (b)M_c for $0 \le x \leqslant 0.03$; and (c) χ_a and χ_c, and χ_c^{-1} (right scale) for $x = 0.03$. Inset: Enlarged χ_a for both ZFC and FC samples below 15 K.

and 1(c) where the magnitudes and real parts of the complex Fourier-transformed XAFS data (black line) and fits (red line) are plotted, respectively. The local Tb-O, Tb-Sr, and Tb-Ir distances were found to be expanded by 0.10(1), 0.12(4), and 0.05(3) Å relative to the Ir-O, Ir-Sr, and Ir-Ir distances in the undoped structure of Sr_2IrO_4. This is consistent with results from the XANES measurements where Tb is found to be in the tetravalent state (the ionic radius of Tb^{4+} is 0.13 Å larger than that of Ir^{4+} ions in an octahedral environment). The expansion of the bonding distances of Tb can be attributed to the $4f$ electrons: they are localized and have small binding energies, and the S state of the Tb^{4+} f shell is spherical and does not favor directional bonds.

We have based our conclusion that Tb dopants occupy Ir sites on the results of simulations of Tb XAFS data using FEFF 6.0 theoretical standards (Fig. 2). The simulations are remarkably different for Tb doping at Ir and Sr sites. It suffices to inspect the plots in Fig. 2 to conclude that Tb is

located at Ir sites since the simulations in that case reasonably agree with the data even without carrying out any fittings. In contrast, the placement of Tb at Sr sites is inconsistent with the data. The local atomic environments around Ir and Sr sites are very different; hence XAFS can easily detect Tb site substitution. For example, for Tb at Ir sites the peaks in Figs. 2(a) are due to oxygen neighbors, Sr neighbors, and then Ir neighbors with increasing distance from the Tb site. In comparison, for Tb at Sr sites the first peak is due to oxygen neighbors, then Ir neighbors, and then Sr neighbors. As seen in these simulations in Fig. 2, placing Tb dopants at Ir sites yields perfect fits to the data by accommodating small distortions related to mismatch in ionic radii between Tb and Ir ions. The XAFS data cannot be fitted with a model in which Tb atoms replace Sr atoms.

A unique and important structural feature, which is absent in La_2CuO_4, is that Sr_2IrO_4 crystallizes in a reduced tetragonal structure (space-group $I4_1/a$) due to a rotation of the IrO_6 octahedra about the c axis by $\sim 11^\circ$, resulting in a larger unit cell by $\sqrt{2} \times \sqrt{2} \times 2$ [34–38]. This rotation corresponds to a distorted in-plane Ir-O-Ir bond angle θ critical to the electronic structure [9–12]. Slightly substituting Tb^{4+} for Ir^{4+} (up to 3%) retains the tetragonal crystal structure but causes significant changes in the lattice parameters and reduces structural distortions (Fig. 3). The initial decrease in the unit cell volume V is unusual but it is followed by a sudden increase in V at $x = 0.03$, which is anticipated by the increased bonding distances of Tb [Fig. 3(a)]. Similarly, the c/a ratio decreases initially and then rises at $x = 0.03$, roughly tracking the changes in V. Hence, the variation of $V = (c/a)a^3$ with x is predominantly driven by (c/a), i.e., c. It is also remarkable that the rotation of IrO_6-octehedra inherent in Sr_2IrO_4 is considerably reduced so that the Ir-O-Ir bond angle θ increases almost linearly with x from 156.47° at $x = 0$ to 160.05° at $x = 0.02$ before dropping to 158.60° at $x = 0.03$ [Fig. 3(b)]. These changes have important implications for magnetic properties because of the strong magnetoelastic coupling [21,36–40].

Impurities are expected to disrupt the itinerant order of the Ir spins, which is based on collective modes, and destroy the spin-density waves. Localized moments are much less susceptible to impurities. The tetravalent $Tb^{4+}(4f^7)$ ion, similarly to the $Gd^{3+}(4f^7)$ ion, is an S state carrying the total spin and angular momentum $S = 7/2$ and $L = 0$, respectively. The $4f$ electrons are localized and have no crystalline field splitting. As shown in Figs. 4(a) and 4(b), 3% Tb doping effectively suppresses the long-range AFM transition temperature T_N from 240 K at $x = 0$ to zero. There is a kink in $M(T)$ for $x = 0$ at 100 K that is attributed to a possible rearrangement of the magnetic order and is closely associated with magnetoresistivity [23], the magnetoelectric effect [10], and unusual muon responses [38]. For $x = 0.03$, a magnetic hysteresis behavior along with a small kink near 10 K is observed in the a-axis magnetic susceptibility χ_a measured using zero-field-cooling (ZFC) and field-cooling sequences (FC) sequences [see the inset in Fig. 4(c)]; the anomaly is absent in the c-axis magnetic susceptibility χ_c. This behavior suggests an incommensurate magnetic order, and is confirmed by the neutron diffraction discussed below.

Fitting the magnetic data for χ_c in Fig. 4(c) to a Curie-Weiss law for a temperature range of 1.7-320 K for $x = 0.03$

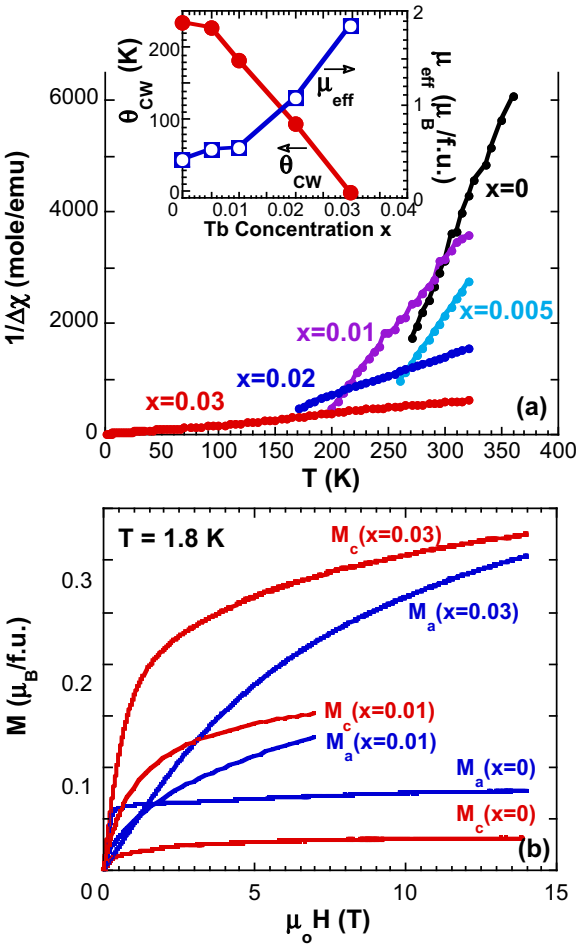

FIG. 5. (Color online) (a) The temperature dependence of $\Delta\chi^{-1}$ for $0 \leqslant x \leqslant 0.03$. Inset: The Tb concentration x dependence of the Curie-Weiss temperature θ_{CW} and effective moment μ_{eff}. (b) The isothermal magnetization M_a (blue) and M_c (red) up to 14 T for $0 \leq x \leqslant 0.03$.

yields the Curie-Weiss temperature $\theta_{CW} = -1.5$ K, consistent with the vanishing T_N. A systematic decrease in θ_{CW} or the exchange coupling with x closely tracks the decreasing T_N, as illustrated in Fig. 5(a). Extrapolation of $\theta_{CW}(x)$ to x slightly larger than 0.03 suggests a change of sign. The x dependence of θ_{CW} suggests a vanishing AFM state and an emerging new state with ferromagnetic correlations near $x = 0.03$. An increase in the effective moment μ_{eff} with x is a result of increased Tb doping that enhances μ_{eff} from 0.5 for $x = 0$ to 1.85 μ_B/formula unit (f.u.) for $x = 0.03$ [see Fig. 5(a)]. With $S = 7/2$, the tetravalent $Tb^{4+}(4f^7)$ ion has an effective moment μ_{eff} of 7.94 μ_B/Tb. The greatly enhanced $\mu_{eff}(= 1.85\,\mu_B/\text{f.u.})$ does not scale well at 3% of Tb doping, implying a significant interaction between Ir $5d$ and Tb $4f$ electrons that intensifies μ_{eff}.

Such a strong $5d$-$4f$ interaction also effectively affects the magnetic anisotropy and ordered moment at low temperatures, and this is evidenced in the isothermal magnetization $M(T,H)$ [Fig. 5(b)]. For $x = 0$, the a-axis M_a is more than twice as strong as the c-axis M_c because the magnetic moments lie within the basal plane [37,38]. Upon Tb doping, M_c

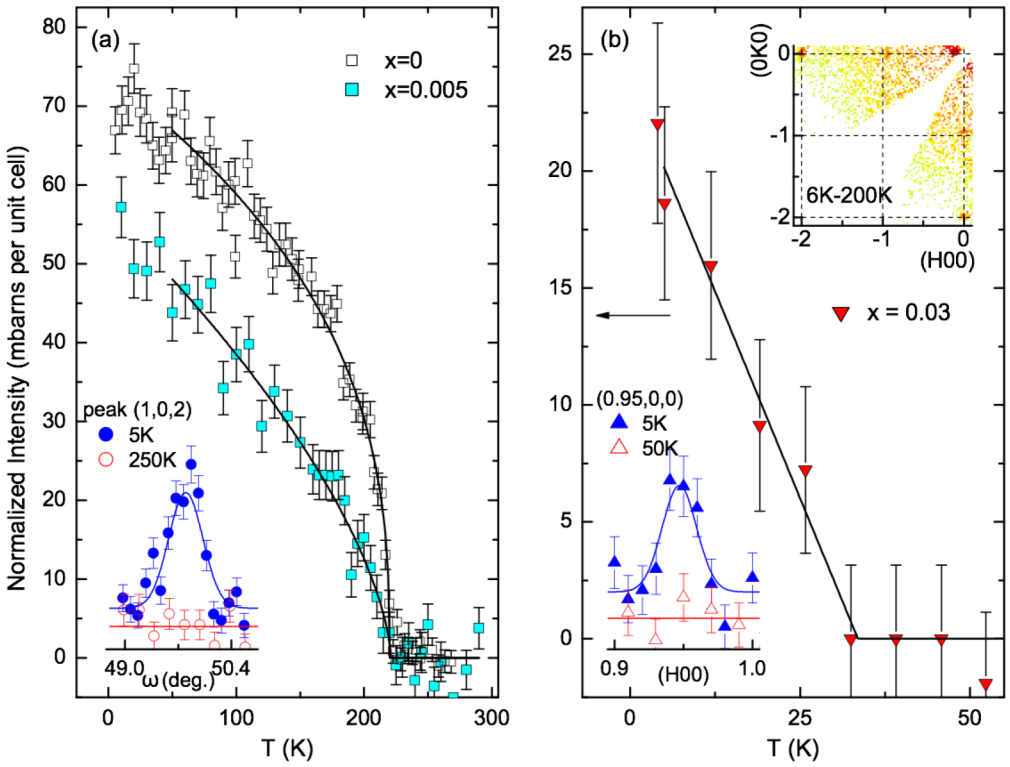

FIG. 6. (Color online) The neutron diffraction results: (a) Temperature dependence of the peak (1,0,2) for $x = 0$ (black) and $x = 0.005$ (cyan). The intensity is normalized to the cross section in units of millibarns per unit cell. Inset: The rocking curve of the (1,0,2) peak for $x = 0.005$ at 5 K (blue) and 250 K (red). (b) Temperature dependence of peaks (0.95,0,0) and (0,0.95,0) for $x = 0.03$ in the same units as in (a). Upper inset: the *HK*0-slice from time-of-flight (TOF) neutron data (on CORELLI). The data at 200 K are subtracted as background. The peak around (1,0,0)/(0,1,0) is slightly away from integer positions. Lower inset: High-resolution triple-axis results (on HB1A) of (*H*,0,0) scan at 5 K (blue) and 50 K (red). Consistently with the TOF result, the peaks are incommensurate at (0.95,0,0) and (0,0.95,0).

becomes larger than M_a instead. $M(H)$ at low temperatures is considerably enhanced because of Tb doping. For example, M_c extrapolated to $H = 0$ for $x = 0.03$ is approximately $0.25\,\mu_B$/f.u at T = 1.8 K, one order of magnitude stronger than $\sim 0.02\,\mu_B$/Ir for $x = 0$. The field dependence of $M(T,H)$ at 1.8 K is also suggestive of ferromagnetic (FM) -like behavior [see Fig. 5(b) as well as Fig. 4]. While for $x = 0$ M saturates already at $\mu_0 H < 2$ T, for $x = 0.03$ the magnetization does not saturate at 14 T.

These changes in the magnetic state are corroborated by results of our neutron diffraction study, as shown in Fig. 6. With increasing x, a signature magnetic peak at (1,0,2) for the AFM state at $x = 0$ [37,38] becomes weakened at $x = 0.005$ [Fig. 6(a)] and eventually vanishes at $x = 0.03$. Note that the magnetic peak intensity at $x = 0.005$ decreases and the magnetic moment is reduced to 90% of that at $x = 0$. The disappearance of the sharp magnetic peak associated with the canted antiferromagnetic configuration at $x = 0$ is accompanied by an emergent incommensurate magnetic order with wave vectors $q_m = (0.95,0,0)$ and (0,0.95,0). The incommensurate magnetic order becomes better defined at $x = 0.03$ when the higher-T background is subtracted [inset of Fig. 6(b)]. The intensity of the new peaks is much weaker compared to those at $q = (1,0,2)$ for $x = 0$. The new peaks exhibit a clear temperature-dependence and evolve into a featureless background above 30 K. The occurrence of the pair of peaks at (0.95,0,0) and (0, 0.95, 0) implies a possible spiral order with moments along the c axis or an incommensurate spin-density wave as neutron diffraction probes only the moment component perpendicular to the momentum transfer. The spiral order along the c axis agrees with the stronger M_c at $x = 0.03$ [Fig. 5(b)] and is therefore the more likely scenario. It is likely that the magnetic moment of Tb ions, which tends to polarize the magnetic moment of surrounding Ir ions along with it, is ferromagnetically aligned along the c axis or forms magnetic polarons. Generally, a c-axis alignment is more energetically favorable when the tetragonal crystal field effect (CFE) is enhanced [14], and specifically the significantly increased c/a ratio at $x = 0.03$ [Fig. 3(b)] inevitably strengthens the tetragonal CEF, thus favoring the c-axis alignment for the Ir moments. In addition, the Hund's rule coupling is also enhanced on the Tb sites, further increasing the tendency of a FM interaction along the c axis. A strong competition between the in-plane AFM (due to Ir *5d* electrons) and out-of-plane FM (due to Tb *4f* electrons) interactions thus accounts for the disappearance of the canted AFM state at $x = 0.03$.

The a-axis and c-axis electrical resistivity, $\rho_a(T)$ and $\rho_c(T)$, are systematically reduced with x. $\rho_a(T)$ decreases by nearly four orders of magnitude at low temperatures from $\sim 10^6\,\Omega$ cm at x = 0 to $\sim 10^2\,\Omega$ cm at $x = 0.03$, as shown in Figs. 7(a) and 7(b). The reduction of $\rho_a(T)$ and $\rho_c(T)$ may be

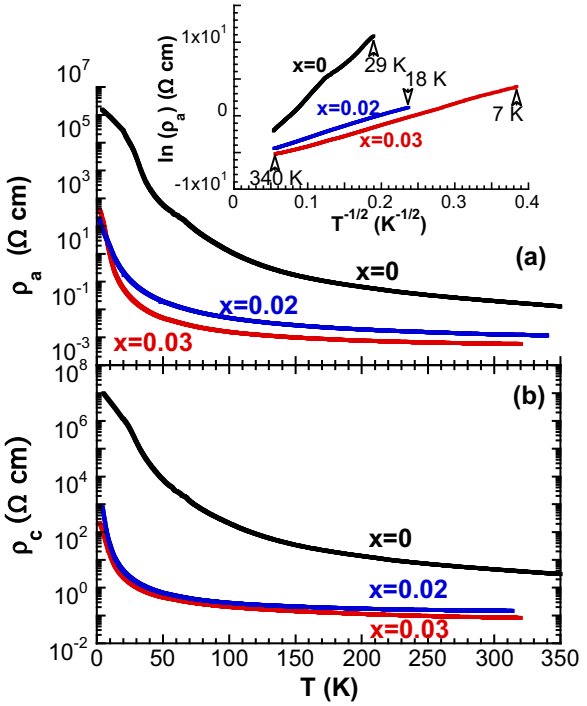

FIG. 7. (Color online) The temperature dependence of (a) the a-axis resistivity ρ_a and (b) the c-axis resistivity ρ_c for $0 \leqslant x \leqslant 0.03$. Inset: $\ln(\rho_a)$ vs $T^{-1/2}$ for $x = 0$, 0.02 and 0.03.

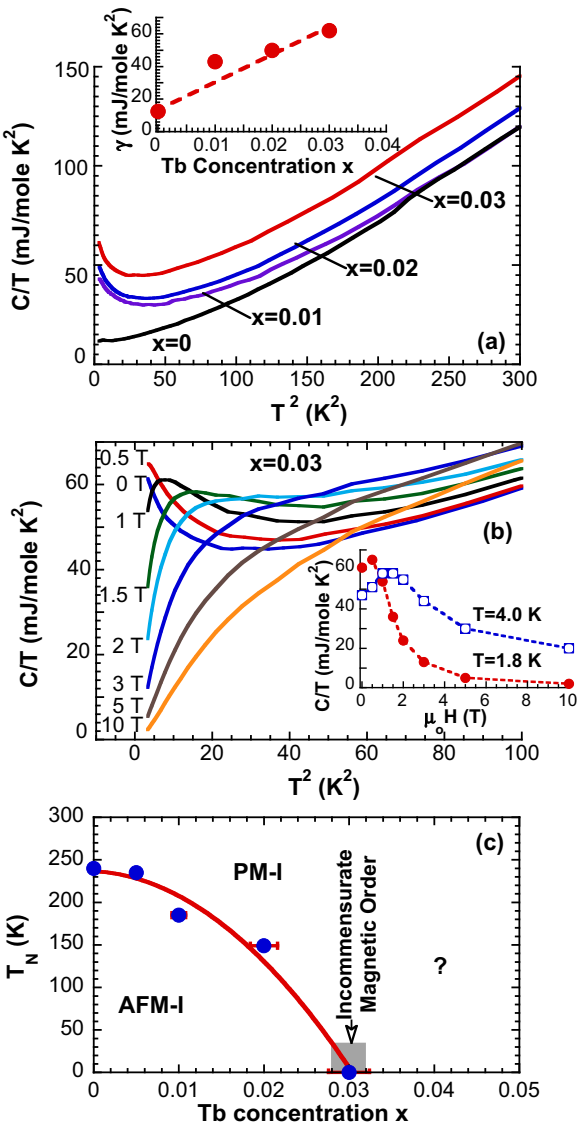

FIG. 8. (Color online) (a) The specific heat $C(T)/T$ vs T^2 for $0 \leqslant x \leqslant 0.03$ and $1.7 < T < 18$ K. Inset: $C(T)/T$ or γ at $T = 1.8$ K vs .(b)$C(T)/T$ vs T for $x = 0.03$ at representative magnetic fields $\mu_0 H$ up to 14 T. Inset: $C(T)/T$ or γ vs $\mu_0 H$. (c) The phase diagram for $Sr_2Ir_{1-x}Tb_xO_4$ generated based on the data presented above. Note that PM-I stands for a paramagnetic insulator and AFM-I for an antiferromagnetic insulating state.

a result of the increased Ir-O-Ir bond angle θ, which makes electron hopping more energetically favorable. However, the insulating state remains at $x = 0.03$ with both $d\rho_a/dT$ and $d\rho_c/dT < 0$. Indeed, the ratio of $\rho(2\,\mathrm{K})/\rho(300\,\mathrm{K})$ for $\rho_a(T)$ merely drops by one order of magnitude, from $\sim 10^6$ at $x = 0$ to $\sim 10^5$ at $x = 0.03$; this ratio for $\rho_c(T)$ at $x = 0.03$ is 2500. A close examination of $\rho_a(T)$ and $\rho_c(T)$ reveals that ρ for $x > 0$ follows a variable-range hopping (VRH) model, $\rho \sim \exp(1/T)^{1/2}$, for a remarkably wide temperature range, particularly for $x = 0.03$. To a lesser extent, ρ for $x = 0$ also follows the VRH behavior [see the inset in Fig. 7(a) for $\rho_a(T)$], suggesting that the structural distortion may play a significant role. Nevertheless, the VRH behavior signals that Anderson localization, rather than thermal activation, dominates the hopping process with long-range Coulomb repulsions between carriers playing an important role in this regime [41–43]. Anderson localization, which is due to disorder in general, may be associated with an energy level mismatch for the Ir and Tb sites that ultimately weakens electron hopping and results in the persistent insulating state.

The specific heat $C(T)$ for $5 < T < 20$ K approximately fits a common expression, $C(T) = \gamma T + \beta T^3$, where the first term arises from the electronic contribution to $C(T)$ and the second term the phonon contribution; γ is usually a measure of the density of states of the conduction states near the Fermi surface and effective mass and β is related to the Debye temperature [see Fig. 8(a)]. It is therefore intriguing to have relatively large γ in an insulator. The origin of a specific heat linear in T could be two-level tunneling centers between two atomic positions (possibly for the O ions) due to light disorder in the material even for $x = 0$ [17,18,21,44,45]. The increase of γ or $C(T)/T$ with x despite the persistent insulating state [inset in Fig. 8(a)] is due to the Tb^{4+} spins. Below 5 K, the pronounced upturn in $C(T)/T$ for $x > 0$ and its strong dependence on the magnetic field H which is parallel to the c axis [see Fig. 8(b)] is likely due to the spin degrees of freedom of the Tb^{4+} $S = 7/2$ states. The field-dependence of $C(T)/T$ exhibits a peak that shifts up with increasing temperature when the field is increased [inset in Fig. 8(b)]. This behavior is consistent with weakly correlated Tb^{4+} ions ($S = 7/2$) in a magnetic field. The zero-field entropy $S = \int [C(x = 0.03) - C(x = 0)](dT/T)$ is 0.63 J/mole K. Converted into the entropy per Tb^{4+}- spin, we obtain 2.53 k_B which is only slightly larger than the entropy of an $S = 7/2$, i.e. $[\ln(8)]k_B = 2.08k_B$.

IV. SUMMARY

A phase diagram is constructed based on the results presented above, as shown in Fig. 8(c). In essence, Tb^{4+} substituting for Ir^{4+} alters the relative strength of the SOI and the tetragonal CEF, and enhances the Hund's rule coupling that competes with the SOI. It is the combined effect of these changes that accounts for the complete suppression of the in-plane AFM state and the occurrence of the spiral order with only 3% of Tb doping. However, an energy level mismatch for the Ir and Tb sites and different symmetry to the different energy levels might depress the carrier hopping between an octahedron containing a Tb ion and one with an Ir ion, potentially preventing the simultaneous emergence of a metallic state. Additional tools such as calculations using density functional theory that could provide more insight into carrier hopping across the lattice would be desirable. Nevertheless, this study provides considerable empirical evidence that suggests an unconventional correlation between the AFM and insulating states in which the magnetic transition plays no critical role in the formation of a charge gap in the iridate.

ACKNOWLEDGMENTS

G.C. is grateful to Dr. Ribhu Kaul and Dr. Daniel Khomskii for useful discussions. This work was supported by NSF through Grant No. DMR-1265162 and by the Department of Energy (BES) through Grant No. DE-FG02-98ER45707 (P.S.). Work at Argonne National Laboratory was supported by the U.S. DOE, Office of Science, Office of Basic Energy Sciences under Contract No. DE-AC02-06CH11357. Work at ORNL was sponsored by the Scientific User Facilities Division, Office of Basic Energy Sciences, the U.S. Department of Energy. J.C.W. is grateful for support from the Chinese Scholarship Council.

[1] G. Cao, J. Bolivar, S. McCall, J. E. Crow, and R. P. Guertin, Phys. Rev. B **57**, R11039(R) (1998).
[2] B. J. Kim, Hosub Jin, S. J. Moon, J.-Y. Kim, B.-G. Park, C. S. Leem, Jaejun Yu, T. W. Noh, C. Kim, S.-J. Oh, J.-H. Park, V. Durairai, G. Cao, and E. Rotenberg, Phys. Rev. Lett. **101**, 076402 (2008).
[3] S. J. Moon, H. Jin, K. W. Kim, W. S. Choi, Y. S. Lee, J. Yu, G. Cao, A. Sumi, H. Funakubo, C. Bernhard, and T. W. Noh, Phys. Rev. Lett. **101**, 226402 (2008).
[4] B. J. Kim, H. Ohsumi, T. Komesu, S. Sakai, T. Morita, H. Takagi, and T. Arima, Science **323**, 1329 (2009).
[5] J. Kim, D. Casa, M. H. Upton, T. Gog, Y.-J. Kim, J. F. Mitchell, M. van Veenendaal, M. Daghofer, J. van den Brink, G. Khaliullin, and B. J. Kim, Phys. Rev. Lett. **108**, 177003 (2012).
[6] S. Fujiyama, H. Ohsumi, T. Komesu, J. Matsuno, B. J. Kim, M. Takata, T. Arima, and H. Takagi, Phys. Rev. Lett. **108**, 247212 (2012).
[7] Q. Wang, Y. Cao, J. A. Waugh, S. R. Park, T. F. Qi, O. B. Korneta, G. Cao, and D. S. Dessau, Phys. Rev B **87**, 245109 (2013).
[8] Jixia Dai, Eduardo Calleja, G. Cao, and Kyle McElroy, Phys. Rev. B **90**, 041102(R) (2014).
[9] O.B. Korneta, Tongfei Qi, S. Chikara, S. Parkin, L. E. DeLong, Pedro Schlottmann, and G. Cao, Phys. Rev. B **82**, 115117 (2010).
[10] M. Ge, T. F. Qi, O. B. Korneta, D. E. De Long, P. Schlottmann, W. P. Crummett, and G. Cao, Phys. Rev. B **84**, 100402(R) (2011)
[11] T. F. Qi, O. B. Korneta, L. Li, K. Butrouna, V. S. Cao, Xiangang Wan, P. Schlottmann, R. K. Kaul, and G. Cao, Phys. Rev. B **86**, 125105 (2012).
[12] S. J. Yuan, S. Aswartham, J. Terzic, H. Zheng, H. D. Zhao, P. Schlottmann, and G. Cao, Phys. Rev. B **92**, 245103 (2015).
[13] F. Wang and T. Senthil, Phys. Rev. Lett. **106**, 136402 (2011).
[14] G. Jackeli and G. Khaliulin, Phys. Rev. Lett. **102**, 017205 (2009).
[15] Hiroshi Watanabe, Tomonori Shirakawa, and Seiji Yunoki, Phys. Rev. Lett. **105**, 216410 (2010).
[16] Y. K. Kim, O. Krupin, J. D. Denlinger, A. Bostwick, E. Rotenberg, Q. Zhao, J. F. Mitchell, J. W. Allen, and B. J. Kim, Science **345**, 187 (2014).
[17] O. B. Korneta, S. Chikara, S. Parkin, L. E. DeLong. P. Schlottmann, and G. Cao, Phys. Rev. B **81**, 045101 (2010).
[18] L. Li, T. F. Qi, L. S. Lin, X. X. Wu, X.T. Zhang, K. Butrouna, V. S. Cao, Y. H. Zhang, J. Hu, S. J. Yuan, P. Schlottmann, L. E. DeLong, and G. Cao, Phys. Rev. B **87**, 174510 (2013).
[19] D. Haskel, G. Fabbris, Mikhail Zhernenkov, P. P. Kong, C. Q. Jin, G. Cao, and M. van Veenendaal, Phys. Rev. Lett. **109**, 027204 (2012).
[20] D. A. Zocco, J. J. Hamlin, B. D. White, B. J. Kim, J. R. Jeffries, S. R. Weir, Y. K. Vohra, J. W. Allen, and M. B. Maple, J. Phys.: Condens. Matter **26**, 255603 (2014).
[21] S. Chikara, O. Korneta, W. P. Crummett, L. E. DeLong, P. Schlottmann, and G. Cao, Phys. Rev. B **80**, 140407(R) (2009).
[22] G. Cao, Y. Xin, C. S. Alexander, J. E. Crow, P. Schlottmann, M. K. Crawford, R. L. Harlow, and W. Marshall, Phys. Rev. B **66**, 214412 (2002).
[23] G. Cao, J. E. Crow, R. P. Guertin, P. Henning, C. C. Homes, M. Strongin, D. N. Basov, and E. Lochner, Solid State Commun. **113**, 657 (2000)
[24] D. Hsieh, F. Mahmood, D. H. Torchinsky, G. Cao, and N. Gedik, Phys. Rev. B **86**, 035128 (2012).
[25] Q. Li, G. Cao, S. Okamoto, J. Yi, W. Lin, B. C. Sales, J. Yan, R. Arita, J. Kuneš, A. V. Kozhevnikov, A. G. Eguiluz, M. Imada, Z. Gai, M. Pan, and D. G. Mandrus, Sci. Rep. **3**, 3073 (2013).
[26] Nevill Mott, *Metal-Insulator Transitions* (Taylor and Francis, London, 1990).
[27] G. M. Sheldrick, Acta Crystallogr., Sect. A: Found. Adv. A **64**, 112 (2008).
[28] J. Rodriguez-Carvajal, Physica B **192**, 55 (1993).
[29] See Supplemental Material at http://link.aps.org/supplemental/10.1103/PhysRevB.92.214411 for an example of the EDX results with standard deviation.
[30] S. I. Zabinsky, J. J. Rehr, A. Ankudinov, R. C. Albers, and M. J. Eller, Phys. Rev. B **52**, 2995 (1995).
[31] H. Fujishiro, T. Naito, D. Takeda, N. Yoshida, T. Watanabe, K. Nitta, J. Hejtmánek, K. Knížek, and Z. Jirák, Phys. Rev. B **87**, 155153 (2013).

[32] G. Fabbris, T. Matsuoka, J. Lim, J. R. L. Mardegan, K. Shimizu, D. Haskel, and J. S. Schilling, Phys. Rev. B **88**, 245103 (2013).
[33] Gang Cao and Lance E. De Long, *Frontiers of 4d- and 5d-Transition Metal Oxides* (World Scientific, Singapore, 2013), p. 269.
[34] M. K. Crawford, M. A. Subramanian, R. L. Harlow, J. A. Fernandez-Baca, Z. R. Wang, and D. C. Johnston, Phys. Rev. B **49**, 9198 (1994).
[35] R. J. Cava, B. Batlogg, K. Kiyono, H. Takagi, J. J. Krajewski, W. F. Peck, Jr., L. W. Rupp, Jr., and C. H. Chen, Phys. Rev. B **49**, 11890 (1994)
[36] M. A. Subramanian, M. K. Crawford, R. L. Harlow, T. Ami, J. A. Fernandez-Baca, Z. R. Wang, and D. C. Johnston, Physica C **235-240**, 743 (1994)
[37] Feng Ye, Songxue Chi, Bryan C. Chakoumakos, Jaime A. Fernandez-Baca, Tongfei Qi, and G. Cao, Phys. Rev. B **87**, 140406(R) (2013)
[38] F. Ye, X. Wang, C. Hoffmann, J. Wang, S. Chi, M. Matsuda, B. C. Chakoumakos, J. A. Fernandez-Baca, and G. Cao, Phys. Rev. B **92**, 201112(R) (2015).
[39] D. H. Torchinsky, H. Chu, L. Zhao, N. B. Perkins, Y. Sizyuk, T. Qi, G. Cao, and D. Hsieh, Phys. Rev. Lett. **114**, 096404 (2015).
[40] I. Franke, P. J. Baker, S. J. Blundell, T. Lancaster, W. Hayes, F. L. Pratt, and G. Cao, Phys. Rev. B **83**, 094416 (2011).
[41] A. L. Efros and B. L. Shklovskii, J. Phys.. C **8**, L49, (1975).
[42] Nevill Mott, *Metal-Insulator Transitions* (Ref. [26]), p. 52.
[43] P. A. Cox, *Transition Metal Oxides*, (Clarendon Press, Oxford, 1995), p.198.
[44] N. S. Kini, A. M. Strydom, H. S. Jeevan, C. Geibel, and S. Ramakrishnan, J. Phys.: Condens. Matter **18**, 8205 (2006).
[45] S. A. Carter, B. Batlogg, R. J. Cava, J. J. Krajewski, W. F. Peck, Jr., and L. W. Rupp, Jr., Phys. Rev. B **51**, 17184 (1995).